Double-defect-induced polarization enhanced O_V-BiOBr/$Cu_{2−x}$S high-low junction for boosted photoelectrochemical hydrogen evolution

Xibao Li [a,*], Qiang Liu [a], Fang Deng [b], Juntong Huang [a], Lu Han [c], Chaozheng He [d,*], Zhi Chen [a], Yidan Luo [a], Yongfa Zhu [e,*]

[a] School of Materials Science and Engineering, Nanchang Hangkong University, Nanchang 330063, China
[b] Key Laboratory of Jiangxi Province for Persistent Pollutants Control and Resources Recycle, Nanchang Hangkong University, Nanchang 330063, China
[c] School of Materials and Metallurgy, University of Science and Technology Liaoning, Anshan 114051, China
[d] Institute of Environmental and Energy Catalysis, School of Materials Science and Chemical Engineering, Xi'an Technological University, Xi'an, Shaanxi 710021, China
[e] Department of Chemistry, Tsinghua University, Beijing 100084, China

ARTICLE INFO

ABSTRACT

In order to improve the carrier transfer driving force and separation efficiency, O_V-BiOBr/$Cu_{2−x}$S high-low junction with double defects (Oxygen vacancy and Copper vacancy) was successfully prepared by a facile two-step solvothermal in situ growth technique. O_V-BiOBr/$Cu_{2−x}$S-0.2 showed the highest hydrogen evolution rate (509.75 μmol·cm^{-2}·h^{-1}), which was 12.45, 6.94 and 3.44 times that of pure BiOBr, O_V-BiOBr and BiOBr/ $Cu_{2−x}$S composite, respectively. Obvious free radicals (·OH and ·O_2^-) were observed in the dark state for the first time. Theoretical and experimental results demonstrate that the charge imbalance within O_V-BiOBr/$Cu_{2−x}$S intensifies after the introduction of the double defects, resulting in enhanced interfacial polarization phenomena. Boosted photoelectrochemical hydrogen evolution activities were achieved with the synergistic effect of the internal electric field and polarization electric field. This study will lay a scientific and experimental foundation for the preparation of high-performance photoelectrochemical anode materials with double defect heterojunction.

1. Introduction

Environmental pollution and energy shortage have become the sword of Damocles over people's heads, and carbon peak and neutrality targets have been proposed. Photoelectrochemical (PEC) water splitting has attracted much attention as an environmentally friendly technology that can effectively achieve this goal by capturing solar energy to produce clean energy (hydrogen) [1–3]. However, the slow oxygen evolution reaction on the photoanode is a major obstacle to improving the efficiency of photoelectrochemical hydrogen evolution due to its slow kinetics (4-electron transfer process) and uphill reaction thermodynamics (high energy barrier for O-O bond formation) [4,5]. In recent decades, various photocatalysts have been developed to improve water splitting performance, such as Ir/Ru-based oxides, WO_3, $BiVO_4$, Fe_2O_3, etc. However, their application is limited by not so high carrier separation efficiency and random non directional carrier transmission [6–12]. In the photoelectrochemical water splitting process, carrier separation and transport are in a key position, and the introduction of

defects, construction of heterojunctions, doping and loading of co-catalysts have been proven to be very effective strategies [13–16].

Oxygen vacancy (O_V), as a common defect, has made a splash in recent years because of its excellent properties such as the ability to reduce the bandgap and thus improve the optical absorption and charge separation efficiency of the material, and the ability to act as a capture center for electrons and thus reduce the electron-hole recombination rate [17,18]. Wang et al. obtained a charge transfer rate of 92.2% and a photocurrent density of 5.54 mA/cm^2 at 1.23 V vs. RHE under AM 1.5 G irradiation when constructing O_V in situ in the $BiVO_4$ photoanode and loading NiFeOx oxygen evolution cocatalyst [19]. Zhu et al. developed an O_V-WO_3 catalyst with an oxygen evolution rate of 683 μmol·h^{-1}·g^{-1}, which was 4.3 times that of pure WO_3, attributing to the O_V that can generate electron trapping states to inhibit the direct recombination of photogenerated carriers [20]. Zhang et al. introduced O_V into Fe_2O_3 photoanodes via a simple solvothermal method, and the photocurrent density of Eg-Fe_2O_3 photoanodes could reach 2.8 mA/cm^{-2} at 1.23 V vs. RHE that was 28 times that of untreated Fe_2O_3 photoanodes, which was

---

* Corresponding authors.
E-mail addresses: lixibao@nchu.edu.cn (X. Li), hecz2019@xatu.edu.cn (C. He), zhuyf@mail.tsinghua.edu.cn (Y. Zhu).

attributed to the fact that the introduction of O_V significantly increased the conductivity of Fe_2O_3 photoanodes and reduced the charge transfer resistance between the catalytic material and the electrolyte [21].

In recent years, heterojunction semiconductors have gained rapid development in the field of water splitting due to their abilities to greatly reduce the carrier recombination rate by achieving spatial separation of electrons and holes [22–29]. Xia et al. constructed the Z-scheme Cu_3P/ZIS heterojunction photocatalyst with excellent hydrogen evolution performance by a simple solution-phase hybridization method, and the hydrogen evolution rate could reach 2256.1 $\mu mol \cdot h^{-1} \cdot g^{-1}$, which was 5.2 times that of pure $ZnIn_2S_4$. The reason for the performance improvement was due to the effective separation and migration of carriers caused by the formation of Z- scheme heterojunction and internal electric field (IEF) [30]. Peela et al. successfully synthesized $5CdS/MnO_x$-$BiVO_4$ photocatalysts with an AQY of 11.3% at $\lambda = 420$ nm and a hydrogen evolution rate of 1.01 $mmol \cdot h^{-1} \cdot g^{-1}$. This was due to the formation of S-scheme heterojunction between MnOx-$BiVO_4$ and CdS, which improved the separation efficiency of carriers [31]. Recently, Li et al. constructed type I high-low junction CN/rGO@BPQDs composites with efficient photocatalytic activity, in which the photo-generated holes on the CN could not be transferred to the BPQDs under the action of the IEF and band bending, resulting in the effective separation of e^- and h^+, providing a new idea for the design of heterojunction photocatalysts.

Generally, for n-type semiconductors with photoelectric anodes, holes as minority carriers must be transmitted in the effective space charge region in order to obtain high PEC performance. The reported methods such as heteroatom doping and oxygen vacancy regulation are effective in alleviating the bulk recombination of semiconductor charges, and many strategies will only promote electron transfer. However, the problems of surface recombination of charges and random non-directional transport of carriers have not been effectively solved. Therefore, improving the hole transfer and accelerating the electron-hole separation are effective strategies to enhance the hydrogen-resolving ability. In contrast, as a hole transport material containing Cu vacancy (V_{Cu}), $Cu_{2-x}S$ has very excellent hole transport ability, which is expected to solve this challenge [32]. However, there are few ways to regulate carrier transport from the perspective of enhancing heterojunction space charge polarization, especially the construction of double-defect-induced heterojunction space charge polarization.

Herein, this work proposes to use double defect engineering to construct high-low junction photoelectric anodes based on double-defect-induced polarization enhancement. By selecting appropriate energy band structure matching materials (O_V-BiOBr and $Cu_{2-x}S$) and double defect ratio or relative content, the theoretical basis for the construction of double defect site polar high-low junction photoelectric anode is studied, and the effects of double defect relative content, structure and concentration on the dynamic charge separation and migration of polar high-low junction are explored.

2. Experimental

2.1. Preparation of O_V-BiOBr

In a typical synthesis process, 1 mmol $Bi(NO_3)_3 \cdot 5H_2O$ was added to 15 mL of ethylene glycol (EG) and stirred for 30 min as solution A. Similarly, 1 mmol KBr was added to 15 mL of EG and stirred for 30 min as solution B. B was slowly added dropwise to A and stirred for 1 h. The product was then transferred to a 50 mL Teflon-lined stainless-steel autoclave, sealed and heated at 180 °C for 24 h. After natural cooling to room temperature, the precipitate was collected by centrifugation and washed several times with deionized water and ethanol. Finally, the obtained product was dried in vacuum at 80 °C for 10 h. BiOBr without oxygen vacancies was prepared in water (30 mL) according to the above steps.

2.2. Preparation of $Cu_{2-x}S$

1 mmol $CuCl_2 \cdot 2 H_2O$ was added to 40 mL of EG and stirred until completely dissolved. Subsequently, 1.5 mmol of thioacetamide (CH_3CSNH_2, TAA) was added and stirred vigorously for 2 h until the solution turned yellowish green. The solution was then transferred to a 50 mL Teflon-lined stainless-steel autoclave and heated at 180 °C for 24 h. After natural cooling to room temperature, the product was washed several times with deionized water and ethanol and the precipitate was collected by centrifugation. After drying at 80 °C for 10 h, the product obtained was $Cu_{2-x}S$.

2.3. Preparation of O_V-BiOBr/$Cu_{2-x}S$

O_V-BiOBr/$Cu_{2-x}S$ was synthesized by a two-step solvothermal method. It was similar to the synthesis of $Cu_{2-x}S$ by adding different molarities of O_V-BiOBr and undergoing the same process to obtain O_V-BiOBr/$Cu_{2-x}S$-X (X is the molar ratio of $Cu_{2-x}S$ to O_V-BiOBr, X = 0.1, 0.2, 0.3).

2.4. Characterization

The phase composition and crystal structure of the photocatalysts were determined by Bruker D8 Advance X-ray diffraction (XRD) with Cu Kα radiation in the range of 10–80°. The microscopic morphology and lattice structure of the photocatalysts were characterized by FEI Talos F200X transmission electron microscopy (TEM). X-ray photoelectron spectroscopy (XPS) was measured with Al Kα radiation on Shimadzu Axis Ultra DLD X-ray photoelectron spectroscopy. The radicals and defects were determined by JES-FA200 ESR spectrometer. Ultraviolet-visible diffuse reflectance spectroscopy was performed using Shanghai Metash UV-9000 UV-Vis spectrophotometer. Electrochemical impedance tests (EIS) were performed at open-circuit potentials in the frequency range of $0.1-10^4$ Hz. Mott-Schottky (M-S) data was obtained for three frequencies selected from $-1-1$ V vs. Ag/AgCl with an AC amplitude of 10 mV. The photocurrent-time curve (I-T) was tested at 1.23 V vs. RHE using a 300 W xenon lamp (PLS-SXE 300, Beijing Perfect Light, Beijing, China) as the light source with a 50 s on/off interval. Photocurrent density-potential (J-V) curves were obtained by linear scanning voltammetry at a scan rate of 2 $mV \cdot s^{-1}$ in the voltage range of 1.0–1.6 V vs. RHE with an electrolyte solution of 1 mol/L KOH and 0.5 mol/L Na_2SO_3 (pH=13.6).

2.5. Photocatalytic and photoelectrochemical measurements

The photoelectrochemical performance was performed on a three-electrode electrochemical workstation based on an electrochemical workstation (Chenhua CHI760E, Shanghai, China). Working electrodes were prepared on carbon paper (1 × 1.5 cm). The carbon sheets were treated with ethanol, 18 mol/L H_2SO_4, 0.1 mol/L H_2SO_4 and deionized water in turn. 4 mg of sample powder was uniformly dispersed in 0.5 mL of isopropanol and 0.5 mL of deionized water, and then coated on the surface of the treated carbon sheet (effective area 1 cm^2, the rest was encapsulated using 5 wt% Nafion). The prepared carbon sheet, Pt sheet and saturated Ag/AgCl electrode were used as the working electrode, counter electrode and reference electrode, respectively. 0.5 M sodium sulfate (Na_2SO_4, pH=7) was used for the electrolyte solution. The test potential (Vs. Ag/AgCl) was converted to a reversible hydrogen electrode (E_{RHE}) according to the NERNST equation :
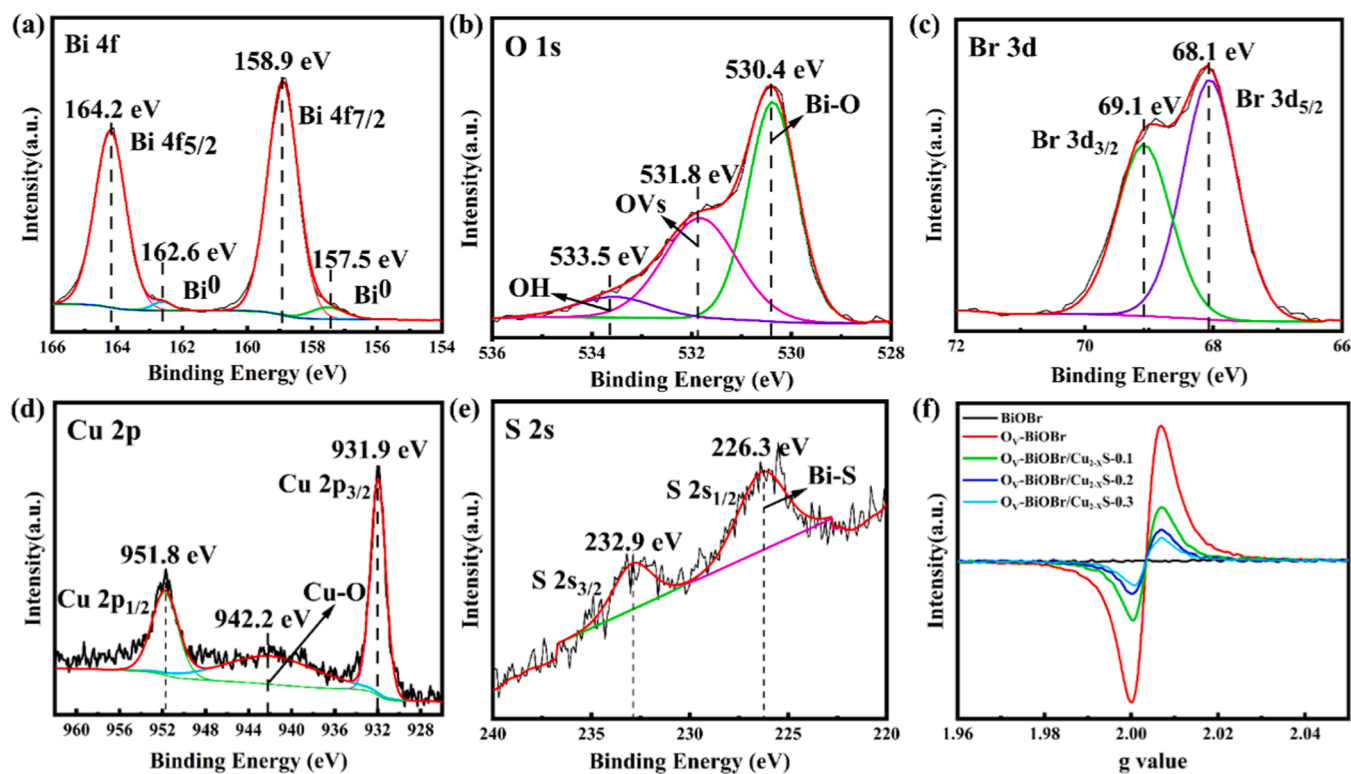
$$E(vs. \quad RHE) = E(vs.Ag/AgCl) + E_{Ag/AgCl}(reference) + 0.059 \times pH \quad (1)$$

where E_{RHE} is the conversion potential to RHE and $E_{Ag/AgCl}$ represents the experimental result to Ag/AgCl, $E_{Ag/AgCl}$ (reference) is 0.197 V at 25 °C.

The photochemical water splitting reaction was carried out in a
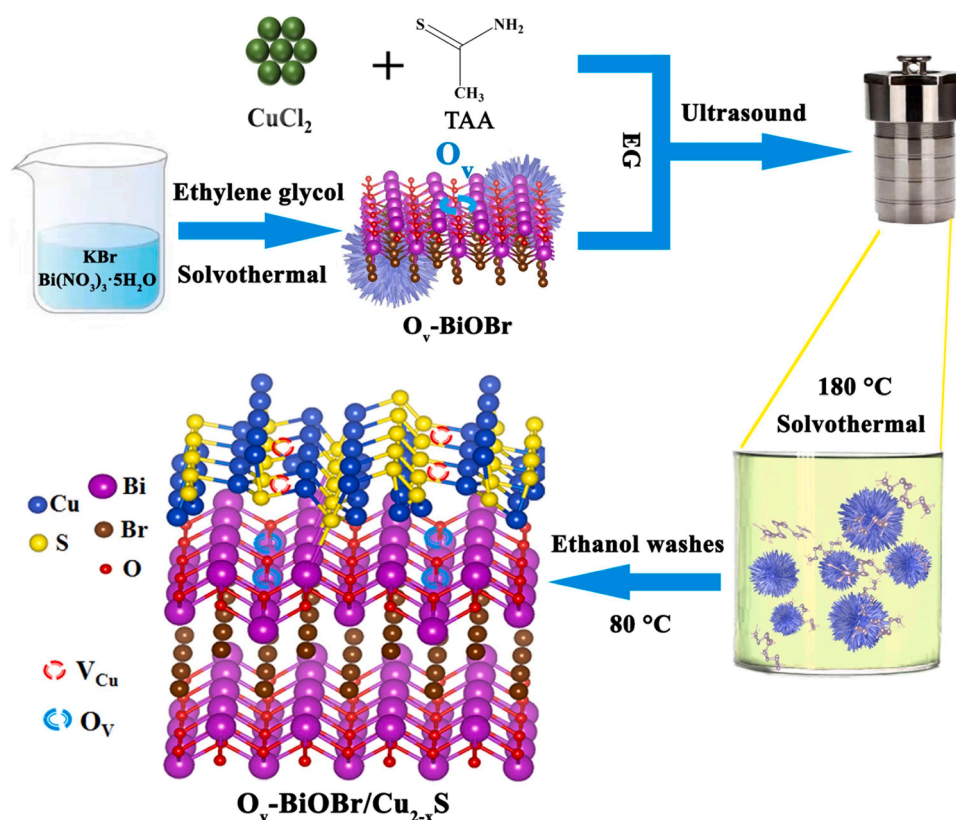
Scheme 1. Schematic diagram of the two-step solvothermal synthesis of O_V-BiOBr/$Cu_{2-x}S$.
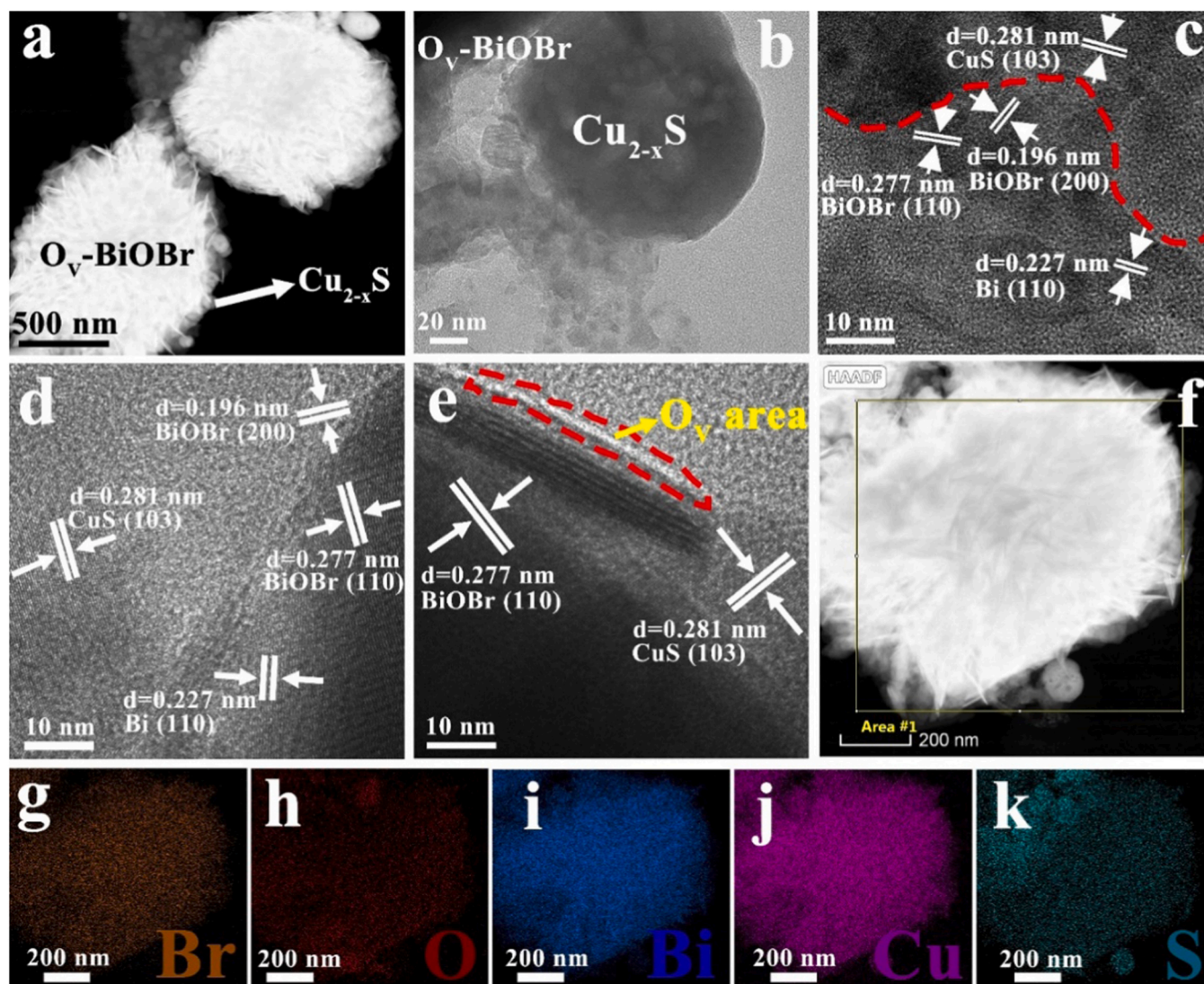

Fig. 1. XPS spectra of (a) Bi 4f, (b) O 1s, (c) Br 3d, (d) Cu 2p, (e) S 2s in O_V-BiOBr/$Cu_{2-x}S$ and (f) EPR spectra of BiOBr and O_V-BiOBr/$Cu_{2-x}S$ with different contents of $Cu_{2-x}S$.

Fig. 2. (a) TEM image and (b-e) HRTEM images of O_V-BiOBr/Cu_{2-x}S, EDS mapping of (g) Br, (h) O, (i) Bi, (j) Cu, (k) S elements in Fig. 1(f).

three-electrode system using an O_V-BiOBr/Cu_{2-x}S electrode (1 × 1 cm^2), a platinum rod, and saturated calomel electrode (SCE) as the working, counter, and reference electrodes, respectively. The electrolyte was 1 mol/L KOH solution (pH 13.6), and 0.5 mol/L Na_2SO_3 was used as the cavity sacrificial agent. The electrolyte was evacuated and subjected to multiple gas washing operations prior to the test. A 300 W xenon lamp (MC-PF300, Beijing Merry Change Technology Co., Ltd) was used as the light source, a bias voltage of 0.55 V was applied, and the amount of hydrogen gas produced was measured every half hour using an automatic on-line vacuum photocatalytic system (MC-SPB10, Beijing Merry Change Technology Co., Ltd) and a gas chromatograph (GC9720II, Zhejiang Fuli Analytical Instruments Co., Ltd).

3. Results and discussion

3.1. Structural and morphological characterizations

O_V-BiOBr/Cu_{2-x}S was successfully prepared using a two-step solvothermal method (as shown in Scheme 1). The crystal structures and crystallinity of O_V-BiOBr, Cu_{2-x}S and O_V-BiOBr/Cu_{2-x}S were investigated using XRD analysis. As shown in Fig. S1(a), the presence of O_V-BiOBr (JCPDS#09–0393), CuS (JCPDS#06–0464) and Bi (JCPDS#85–1329) phases can be observed. Under the action of high

temperature and solvation in the solvothermal process, part of the Bi-O bond breaks, resulting in the precipitation of some Bi elements from the original position of the BiOBr lattice [33]. The diffraction peaks at 2θ = 27.1° and 39.6° correspond to the (012) and (110) planes of Bi phase, respectively. After the coupling of O_V-BiOBr and Cu_{2-x}S, the characteristic peaks corresponding to two pure substances can also be successfully observed, confirming their stable crystal structure. Moreover, as shown in Fig. S1(b), the diffraction peak of O_V-BiOBr/Cu_{2-x}S at (001) plane is significantly shifted and the diffraction intensity is obviously enhanced comparing with that of O_V-BiOBr, which indicates that a strong interfacial interaction is generated between O_V-BiOBr and Cu_{2-x}S, and the two-step solvothermal treatment can significantly improve the crystallinity of O_V-BiOBr, and a novel O_V-BiOBr/Cu_{2-x}S high-low junction composite was successfully prepared.

The chemical valence states and element information of the synthesized samples were examined using X-ray photoelectron spectroscopy (XPS). Fig. S2 shows the full spectrum of O_V-BiOBr/Cu_{2-x}S, which confirms the presence of Bi, O, Br, Cu, and S elements. In Fig. 1(a), the characteristic peaks at the binding energy of 158.9 and 164.2 eV of the Bi 4 f spectrum correspond to Bi^{3+} at Bi 4 $f_{7/2}$ and Bi 4 $f_{5/2}$, respectively, while the characteristic peaks at the binding energy of 157.5 eV (Bi 4$f_{7/2}$) and 162.6 eV (Bi 4 $f_{5/2}$) reflect the formation of Bi^0 simple substance [34]. As shown in Fig. 2(b), the O 1 s can be fitted by three peaks at
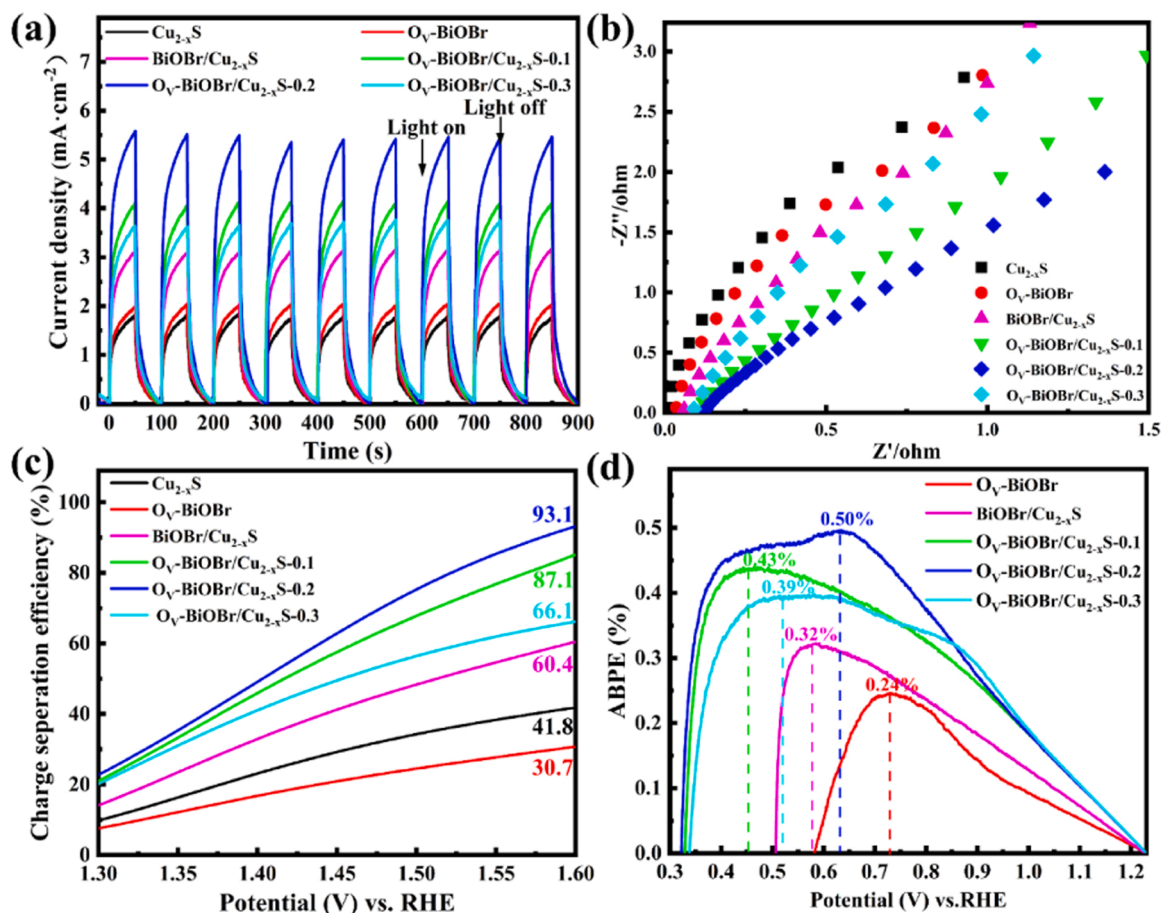
Fig. 3. (a) Transient photocurrent response, (b) Nyquist plots of EIS, (c) calculated charge separation efficiency, (d) ABPE plots.

530.4, 531.8, and 533.5 eV, corresponding to the Bi-O bond, O_V, and -OH groups, respectively [35,36]. Low-temperature solid-state electron paramagnetic resonance (EPR) detection was performed for BiOBr, O_V-BiOBr and different ratios of O_V-BiOBr/Cu_{2-x}S, as shown in Fig. 1(g). All samples except BiOBr display a significant signal at g = 2.002, and the peak intensity of O_V decreased gradually with the increase of Cu_{2-x}S content, indicating that the Cu_{2-x}S content can effectively modulate the concentration of O_V in the composites [18]. The peaks of Br $3d_{5/2}$ and Br $3d_{3/2}$ are correlated with the binding energy appearing at 68.1 and 69.1 eV, respectively (Fig. 1(c)). The XPS spectrum of Cu_{2-x}S is shown in Fig. S3. It illustrates the coexistence of Cu^{2+} and Cu^+ [37]. In Fig. S3(b), the characteristic peak appearing at a binding energy of 169.2 eV is attributed to the sulfate species, indicating the formation of V_{Cu} and confirming the successful synthesis of Cu_{2-x}S [38,39]. As shown in the XPS spectrum of Cu 2p in O_V-BiOBr/Cu_{2-x}S (Fig. 1(d)), the characteristic peaks at binding energies of 951.8 and 931.9 eV are associated with Cu $2p_{1/2}$ and Cu $2p_{3/2}$ of Cu^+, and the appearance of a satellite peak at 942.2 eV is associated with the Cu-O bond, which reflects the coexistence of Cu ions as a monovalent and divalent species [40]. Due to the trace introduction of S and the strong overlap of the peaks of Bi 4 f and S 2p, the two weaker characteristic peaks of S 2 s are located at 226.3 and 232.9 eV, respectively (Fig. 1(e)), which attributes to S 2 $s_{1/2}$ and S 2 $s_{3/2}$, where the characteristic peak with a binding energy of 226.3 eV corresponds to the Bi-S bond [41]. In summary, O_V-BiOBr and Cu_{2-x}S are mainly bonded by Bi-S bonds and Cu-O bonds, indicating that strong chemical bonds are formed between the interface of O_V-BiOBr/Cu_{2-x}S high-low junction. Moreover, the presence of O_V and Bi^0 was successfully detected, which also proves the successful synthesis of O_V-BiOBr/Cu_{2-x}S composites.

The microstructure and elemental distribution of O_V-BiOBr/Cu_{2-x}S

were obtained by high-resolution transmission electron microscopy (HRTEM). As shown in Fig. 2(a-b), O_V-BiOBr/Cu_{2-x}S exhibits a 3D nanosphere structure with CuS nanoparticles of about 160 nm in size anchored on the about 1200 nm microspherical O_V-BiOBr. The obvious contact interface and clear regular lattice stripes can be observed from HRTEM, indicating a strong interaction between O_V-BiOBr and CuS as well as good crystallinity. As shown in Fig. 2(c-e), the crystal planes with interplanar spacings of 0.196 nm and 0.277 nm correspond to the (200) and (110) planes of O_V-BiOBr, respectively. Based on the reported literature, it can be determined that the main exposed crystal plane of BiOBr without oxygen vacancies is the (001) crystal plane [42–44]. The crystal planes with plane spacings of 0.281 nm and 0.227 nm correspond to the (103) crystal plane of CuS and (110) crystal plane of Bi, respectively. Fig. 2(e) demonstrates the irregular lattice observed at the edge of O_V-BiOBr, which can be attributed to the formation of oxygen vacancies [20,45]. Fig. 2(g-k) display the elemental mapping images of O_V-BiOBr/Cu_{2-x}S, showing the presence of five elements such as Br, O, Bi, Cu, and S. The above results indicate that O_V-BiOBr/Cu_{2-x}S complexes with close interfacial contact and stable crystal structure have been successfully synthesized.

3.2. Photoelectrochemical performance

The absorbance and optical band gap of the samples were probed using UV–vis DRS. As shown in Fig. S4(a), the absorbance of O_V-BiOBr was significantly enhanced compared to pure BiOBr and manifested a significant surface plasmon resonance (SPR) effect in the visible range (460–800 nm), which is attributed to the precipitation of Bi metal from O_V-BiOBr [46]. Moreover, the O_V-BiOBr/Cu_{2-x}S composite exhibits stronger photoresponse, especially near-infrared (NIR) light absorption,

Table 1

Comparison of photocurrent density between prepared samples and published catalysts.

SN	Catalyst	Photocurrent density at 1.23 V vs. RHE	Ref.
1	O_V-BiOBr/Cu_{2-x}S	5.45 mA·cm^{-2}	This work
2	Mo:BiVO$_4$/NiFeOOH	4.5 mA·cm^{-2}	[50]
3	Carbon nitride films	119.2 µA·cm^{-2}	[51]
4	WO$_3$/BiVO$_4$@TANiFe	3.7 mA·cm^{-2}	[52]
5	BiVO$_4$/rGO/NiFe-LDH	3.26 mA·cm^{-2}	[53]
6	Co-Pi/Co$_3$O$_4$/Ti:Fe$_2$O$_3$	2.7 mA·cm^{-2}	[54]
7	TiN/N-TiO$_2$	3.12 mA·cm^{-2}	[55]
8	FeCoOx/BiVO$_4$	4.82 mA·cm^{-2}	[56]

which is attributed to the SPR effect of Cu_{2-x}S [47]. Fig. S4(b) shows that the bandgap of BiOBr shrinks from 2.72 eV to 2.56 eV after the introduction of O_V, increasing the absorption of visible light, and the bandgap of Cu_{2-x}S is only 1.40 eV. The valence band (VB) potentials of O_V-BiOBr and Cu_{2-x}S were tested by VB-XPS, which can be calculated by the formula: $E_{NHE} = \varphi + E_{VB-XPS} - 4.44$, where E_{NHE} is the standard hydrogen potential of valence band, E_{VB-XPS} is the VB value measured by VB-XPS and φ is the instrumental work function (4.55 eV) [48]. Therefore, the E_{NHE} of O_V-BiOBr and Cu_{2-x}S is 2.16 eV and 1.24 eV, respectively. The conduction band (CB) potential of O_V-BiOBr (n-type semiconductor) and VB potential of Cu_{2-x}S (p-type semiconductor) can be obtained from the Mott-Schottky (M-S) curve. As shown in Fig. S5 (a-b), the CB potential of O_V-BiOBr and the VB potential of Cu_{2-x}S are − 0.4 and 1.24 eV, respectively. Therefore, the complete band structures of the two materials have been accurately obtained.

The PEC properties of the samples were measured under AM 1.5 G illumination using a mixture of 1 mol/L KOH and 0.5 mol/L Na$_2$SO$_3$ (pH=13.6) as the electrolyte solution. As shown in Fig. 3(a), the O_V-BiOBr/Cu_{2-x}S-0.2 electrode displays a significantly larger photocurrent density than the O_V-BiOBr and BiOBr/Cu_{2-x}S electrodes, reaching a stable photocurrent density value of 5.45 mA/cm^2 at 1.23 V vs RHE, which is 2.87, 3.03 and 1.75 times that of O_V-BiOBr (1.9 mA/cm^2), Cu_{2-x}S (1.8 mA/cm^2) and BiOBr/Cu_{2-x}S (3.11 mA/cm^2), respectively. This improvement stems from the fact that O_V can accelerate electron transport and Cu_{2-x}S can be used as a hole transport channel, thus effectively improving the carrier transport efficiency. This conclusion is supported by the EIS results (Fig. 3(b)). O_V-BiOBr/Cu_{2-x}S-0.2 shows the smallest semicircular diameter, which indicates that the introduction of O_V and the successful compounding of Cu_{2-x}S can effectively reduce the charge transport resistance and improve the charge mobility, but excess

Cu_{2-x}S may become the electron-hole recombination center and reduce the carrier separation efficiency [49]. Compared with the photocurrent density of other photoanode materials, as shown in Table 1, O_V-BiOBr/Cu_{2-x}S exhibits excellent PEC activity. To better understand the charge separation process of samples, the carrier densities were calculated by Equation (6) in the Supporting Information, as shown in Table S1. Compared with the one-component substance, the carrier density is greatly enhanced by the composite of O_V-BiOBr and Cu_{2-x}S, leading to a better charge separation performance. This phenomenon is confirmed in Fig. 3(c), where O_V-BiOBr/Cu_{2-x}S-0.2 exhibits the highest charge separation efficiency of 93.1%, which is 3.03 times that of O_V-BiOBr. In addition, the applied bias photon-to-current efficiency (ABPE) was used to quantify the PEC water oxidation performance of the samples. As shown in Fig. 3(d), O_V-BiOBr/Cu_{2-x}S-0.2 demonstrates a maximum ABPE of 0.5% at 0.62 V vs. RHE, which is 2.1 times that of O_V-BiOBr. Compared with previous work, as shown in Table S2, O_V-BiOBr/Cu_{2-x}S reaches a higher ABPE value, indicating its better photoelectrochemical water splitting performance. In summary, the successful compounding of O_V-BiOBr with Cu_{2-x}S can significantly improve the carrier transport and separation efficiency, which can be effectively improved by regulating the compounding ratio of O_V-BiOBr and Cu_{2-x}S.

The photoelectrochemical hydrogen evolution performance of the samples was tested under visible light using Na$_2$SO$_3$ as a sacrificial agent. Under the action of photoelectricity, oxygen and hydrogen were produced at the cathode and anode, respectively. The measured hydrogen yield is shown in Fig. 4. The O_V-BiOBr/Cu_{2-x}S-0.2 electrode achieves the highest hydrogen generation amount of 1250.9 µmol·cm^{-2}, corresponding to a hydrogen evolution rate of 509.75 µmol·cm^{-2}·h^{-1}, which is 12.45, 6.94 and 3.44 times that of BiOBr (40.94 µmol·cm^{-2}·h^{-1}), O_V-BiOBr (73.47 µmol·cm^{-2}·h^{-1}) and BiOBr/Cu_{2-x}S (147.99 µmol·cm^{-2}·h^{-1}), respectively. The stability of photoelectrochemical hydrogen generation of the samples was also tested, as shown in Fig. 4(a). Under 10 h of continuous light illumination, O_V-BiOBr/Cu_{2-x}S-0.2 still had high hydrogen generation activity after four cycles and maintained high stability. The hydrogen evolution rates are compared with those of some published catalysts, as shown in Table S3, manifesting that O_V-BiOBr/Cu_{2-x}S has better hydrogen evolution performance. In summary, the high PEC activity of O_V-BiOBr/Cu_{2-x}S is attributed to the successful introduction of O_V to promote electron transport and Cu_{2-x}S as a hole transport channel to accelerate the separation and transfer of carriers.

Stability is very important for photoelectrode materials, and corresponding experiments were carried out. As shown in Fig. S7(a), chronoamperometry tests were performed in the presence of a hole sacrificial agent. The photocurrent density of O_V-BiOBr/Cu_{2-x}S has a small change
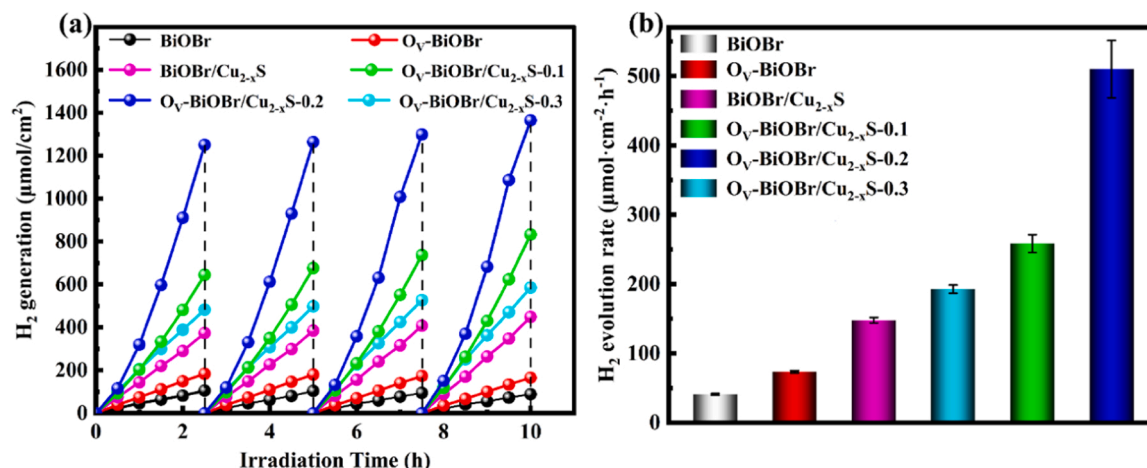

Fig. 4. (a) Hydrogen generation amount and stability, (b) hydrogen evolution rate of the prepared samples.
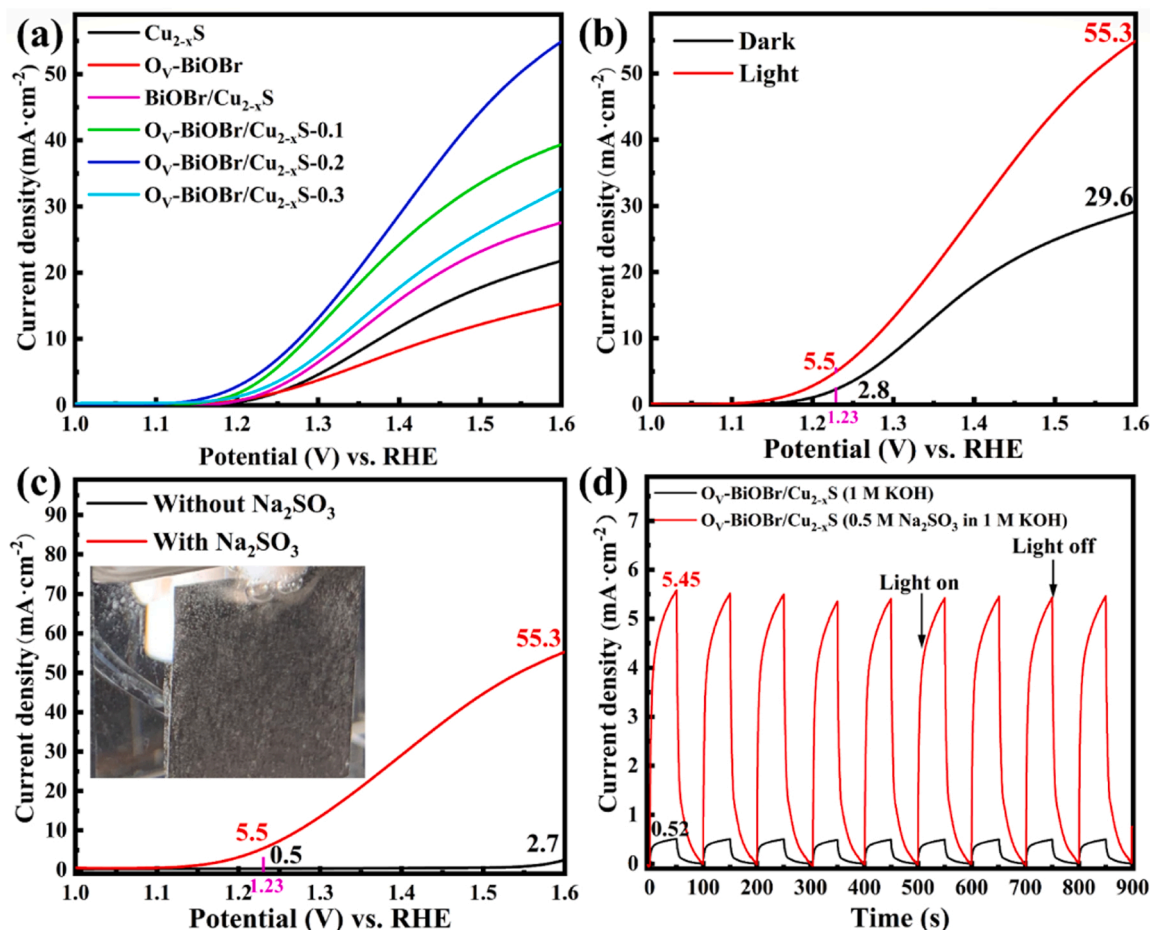
Fig. 5. (a) LSV curves of the samples. (b) LSV curves of O_V-BiOBr/Cu_{2-x}S under illumination and dark. (c) LSV curves of O_V-BiOBr/Cu_{2-x}S with and without the addition of Na_2SO_3. (d) transient photocurrent response of O_V-BiOBr/Cu_{2-x}S (black) in 1 M KOH in the presence of 0.5 mol/L Na_2SO_3 as hole scavenger compared to OVs-BiOBr/Cu_{2-x}S (red) in 1 mol/L KOH only.

range before and after 150 min, indicating its good stability. To study the reaction during proton reduction, the amount of H_2 evolution was measured in a PEC electrolytic cell with an electrolyte of 0.5 mol/L Na_2SO_3 and 1 mol/L KOH under AM 1.5 G illumination, which is compared with the theoretically calculated values. As shown in Fig. S7 (b), the amount of H_2 generated by the O_V-BiOBr/Cu_{2-x}S photoelectrode is close to the theoretical value, and the corresponding Faradaic efficiency is calculated to be about 93%. These results indicate that the electrons on the photoelectrode are almost used to produce H_2, showing that O_V-BiOBr/Cu_{2-x}S has an excellent photoelectrochemical hydrogen evolution performance.

To further understand the effect of environmental factors (such as light illumination and electrolyte solution) on the catalyst performance, corresponding tests were carried out using electrochemical methods. Fig. 5(a) shows the water oxidation performance of the sample at AM 1.5 G. At 1.6 V vs. RHE, O_V-BiOBr/Cu_{2-x}S-0.2 displays the maximum current density of 55.31 mA/cm^2, which is 3.5 times that of O_V-BiOBr (15.69 mA/cm^2). Fig. 5(b) demonstrates the LSV plots of O_V-BiOBr/ Cu_{2-x}S-0.2 under light and dark conditions. At AM 1.5 G, the current density of O_V-BiOBr/Cu_{2-x}S-0.2 at 1.23 V vs. RHE is 5.5 mA/cm^2, which is 1.96 times than that under dark conditions. This indicates that light can effectively promote carrier migration. Fig. 5(c) shows the effect of the hole scavenger on the sample. The performance of O_V-BiOBr/Cu_{2-x}S is greatly improved after using Na_2SO_3 as the hole scavenger, and significant H_2 bubble generation can be observed in the inset. It indicates that the hole scavenger can greatly promote the separation efficiency of electron-hole pairs and thus the carrier mobility, a conclusion supported

by Fig. 5(d). The results manifest a 10.48-fold increase in photocurrent density with the hole scavenger. To investigate the role of Na_2SO_3, photochemical degradation of RhB experiments was performed. As shown in Fig. S6, by using RhB instead of Na_2SO_3 to consume holes, RhB is degraded by nearly 80% at 1 h under a bias voltage of 0.6 V. Moreover, the current density shows a large decrease and then a continuous increase in 1 h, and the current density remains approximately the same before and after 1 h. This is similar to the degradation curve, in the first 10 min, RhB degrades rapidly, generating a large amount of water, and the electrolyte concentration decreases, at which the rate of water generation is larger than that of water decomposition and thus the current density decreases. Subsequently, RhB degrades steadily and water decomposition also proceeds simultaneously, at this time, the rate of water generation is smaller than that of water decomposition. The electrolyte concentration increases slowly, and the current density gradually increases. It indicates that RhB can consume holes and thus promote carrier separation, but the current density in the presence of RhB is much less than that of Na_2SO_3, which indicates that RhB cannot replace Na_2SO_3 as a hole scavenger.

The work function is important to study the charge transfer between O_V-BiOBr and Cu_{2-x}S. The work function (Φ) of O_V-BiOBr, Cu_{2-x}S and O_V-BiOBr/Cu_{2-x}S-0.2 was calculated indirectly using the data measured by VB-XPS. It can be calculated by formula: $\Delta V = \Delta\phi - \varphi$, where ΔV represents the contact potential difference, which is the distance between the two inflection points (IP) of the curve (Fig. S8(a-c)), and φ is the work function of the instrument, which is 4.55 eV [48]. The work functions of O_V-BiOBr, Cu_{2-x}S and O_V-BiOBr/Cu_{2-x}S are obtained as
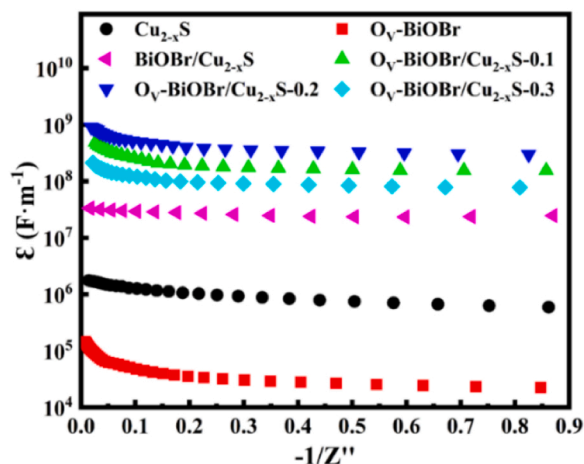
Fig. 6. Dielectric constant versus the imaginary part of the impedance.

5.89, 6.99 and 6.30 eV, respectively. As shown in Fig. S8(d), the Fermi energy level of O_V-BiOBr is higher than that of $Cu_{2-x}S$. When the two materials come into contact, electrons are transferred from the high Fermi energy level of O_V-BiOBr to the low Fermi energy level of $Cu_{2-x}S$ until the Fermi energy level tends to equilibrate [57,58]. At this time, due to the transfer of electrons, an electron depletion layer is formed on the surface of O_V-BiOBr, resulting in its surface being positively charged. Similarly, the surface of $Cu_{2-x}S$ is negatively charged, resulting in the

formation of an IEF pointing from O_V-BiOBr to $Cu_{2-x}S$. Under light irradiation, the IEF promotes the separation of photogenerated electron-hole pairs and accelerates the transfer of holes on the VB of O_V-BiOBr to $Cu_{2-x}S$. Due to the repulsion of the IEF, the electrons on the CB of O_V-BiOBr cannot be transferred to $Cu_{2-x}S$, preserving the highly reducible electrons, which results in efficient PEC hydrogen generation performance. To verify the reduction characteristics of electrons, Cr^{6+} reduction experiments were carried out using methanol as a hole sacrifice. As shown in Fig. S9, Cr^{6+} is difficult to be reduced by methanol without the addition of catalyst. Among them, O_V-BiOBr/$Cu_{2-x}S$ achieves about 62% reduction of Cr^{6+} for 2 h, which is an improvement over O_V-BiOBr. The reduction of electrons and the formation of heterojunctions that can effectively promote electron-hole separation are again verified.

3.3. Relationship between double-defect-induced polarization effect and photoelectrochemical performance

The existence of O_V in O_V-BiOBr and V_{Cu} in $Cu_{2-x}S$ aggravates the non-coincidence of positive (C^+) and negative (C^-) charge centers at the heterojunction interface, resulting in spontaneous enhanced interfacial polarization. To investigate the effects of polarization on the hydrogen evolution performance, the dielectric constant of the samples (Fig. 6) can be calculated by using Eq. (1-5) in the Supporting Information. The dielectric constants all demonstrate large values at low impedances. Compared with pure O_V-BiOBr and $Cu_{2-x}S$, O_V-BiOBr/$Cu_{2-x}S$ complexes illustrate significantly increased dielectric constant, indicating
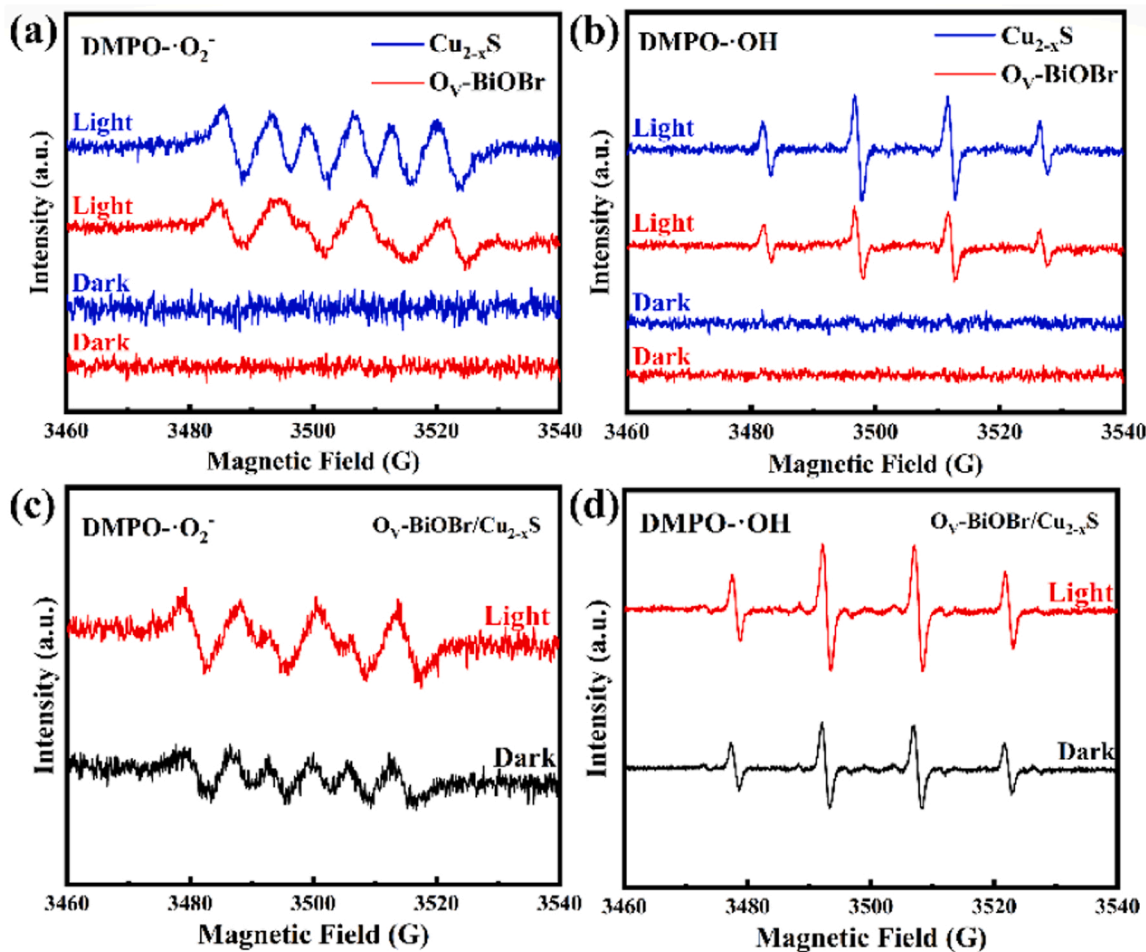

Fig. 7. ESR spectra under dark and visible-light irradiation: (a) DMPO-·O_2^-, (b) DMPO-·OH of O_V-BiOBr and $Cu_{2-x}S$; (c) DMPO-·O_2^-, (d) DMPO-·OH of O_V-BiOBr/$Cu_{2-x}S$.
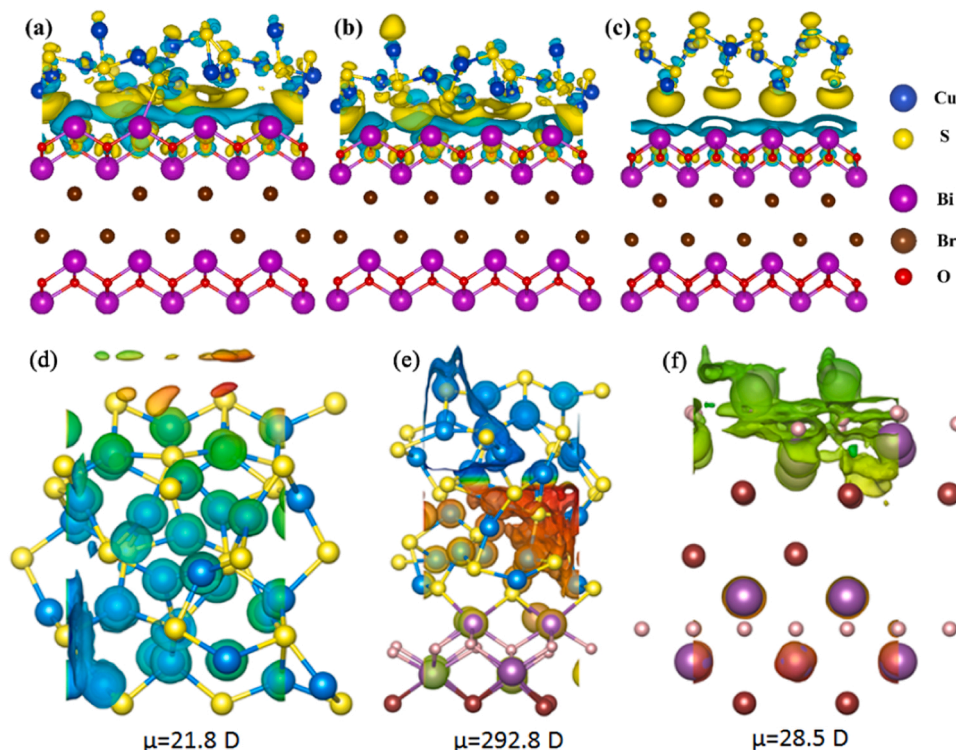
Fig. 8. Difference charge density of (a)O_V-BiOBr/Cu_{2-x}S, (b)BiOBr/Cu_{2-x}S, (c)BiOBr/Cu_2S; diagram of electrostatic potential and dipole moment of (d)Cu_{2-x}S, (e) O_V-BiOBr/Cu_{2-x}S, (f)O_V-BiOBr.

the enhancement of the polarization. Moreover, we found that O_V-BiOBr/Cu_{2-x}S with double defects has higher dielectric constant and polarizability than BiOBr/Cu_{2-x}S with only V_{Cu} but no O_V. The results of electron spin resonance (ESR) of captured radicals validate this conclusion well. As shown in Fig. 7(a-b), neither $\cdot O_2^-$ nor $\cdot OH$ signal is observed in pure O_V-BiOBr and Cu_{2-x}S in the dark state, while the appearance of free radical signals can be observed after light illumination, indicating that only light irradiation can excite free radicals instead of polarization in pure substances at this time. However, in the O_V-BiOBr/Cu_{2-x}S composite, obvious $\cdot O_2^-$ and $\cdot OH$ radicals can be observed in the dark state (Fig. 7(c-d)). These indicate that O_V-BiOBr complexed with Cu_{2-x}S intensifies the charge imbalance phenomenon and the polarization is enhanced. It also implies that the generation of free radicals in the dark state is related to the enhanced polarization, but not to the Fenton-like effect generated by the valence-variable Cu ions. The more significant decrease in the intensity of the electron signal (Fig. S10) after light illumination suggests that photogenerated electrons are also the main active species, and the electrons with high reduction potential are preserved due to the unique advantages of type I high-low junction. The significant enhancement of the electron transfer rate is also due to the polarization enhancement of the heterojunction and the Schottky barrier caused by Bi metal.

3.4. Mechanism analysis of double-defect-induced polarization enhanced photoelectrocatalysis

To reveal how O_V and V_{Cu} affect the charge transfer in O_V-BiOBr/Cu_{2-x}S, the corresponding first-principles calculations were performed. Fig. 8(a-c) shows the effect of double defects (O_V and V_{Cu}) on the charge distribution of heterojunction. After the formation of the heterojunction, electrons mainly concentrate on the Cu_{2-x}S side of the interface. The calculation results illustrate that after introducing double defects into the high-low junction, the charge density difference on both sides of the interface of O_V-BiOBr/Cu_{2-x}S is significantly greater than that of BiOBr/Cu_{2-x}S with single defect and BiOBr/Cu_2S without defect. The value of
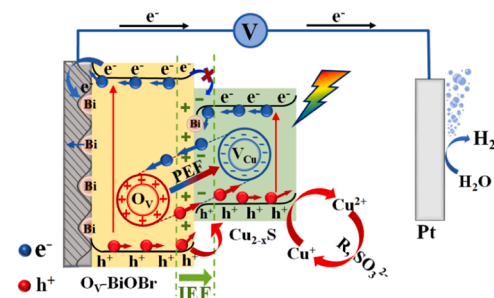

Fig. 9. Schematic diagram of the mechanism of double-defect-induced polarization enhanced O_V-BiOBr/Cu_{2-x}S high-low junction PEC.

dipole moment fitted by the electrostatic potential diagram (Fig. 8(d-f)) also quantitatively confirms that the dipole moment in the O_V-BiOBr/Cu_{2-x}S heterojunction is 13.4 and 10.3 times that of Cu_{2-x}S and O_V-BiOBr respectively, indicating that in addition to the internal electric field at the interface, there is more charge transfer caused by the polarization induced by the double defects. Combined with the dielectric constant conclusion of the material in Fig. 6 (the increase of dielectric constant indicates the enhancement of polarization), it can be deduced that an obvious double-defect-induced space charge polarization is generated in the O_V-BiOBr/Cu_{2-x}S double-defect high-low junction, which is very favorable for charge separation and rapid directional migration along chemically bonded heterointerfaces and the direction of the polarized electric field.

Based on the above experimental results and analysis, a possible mechanism of double-defect-induced polarization enhanced O_V-BiOBr/Cu_{2-x}S high-low junction photoelectrocatalysis for boosted degradation and hydrogen evolution is proposed, as shown in Fig. 9. After the compounding of O_V-BiOBr and Cu_{2-x}S, the highly delocalized positive and negative charges prompt the generation of polarization dipoles, forming a polarization electric field (PEF). At the same time, an IEF

appears at the heterojunction interface, which is mainly caused by the different Fermi levels of the two materials that make up the heterojunction. After light illumination, due to the synergistic effect of the PEF and the IEF, the photogenerated electrons migrate to the O_V-BiOBr side, and the photogenerated holes transfer to the CuS side, realizing efficient space separation and transfer of carriers. At the same time, due to the external bias voltage of PEC and Schottky barrier of Bi metal, the electrons move further towards the substrate and the photocathode. The holes transfer are promoted through the hole enrichment and defect state of V_{Cu}, and the holes can oxidize Cu^+ to Cu^{2+}. While, Cu^{2+} is reduced to Cu^+ again under the action of the hole scavenger Na_2SO_3 and the pollutants, forming a Fenton-like effect and promoting the transport of holes. The existence of the PEF and the IEF allows the retention of the highly reduced electrons on the CB of O_V-BiOBr, and due to the metallicity of Bi, the electrons on O_V-BiOBr and $Cu_{2-x}S$ are transferred to the back electrode through the Schottky barrier of Bi. Under the effect of photoelectricity, the electrons are transferred together with the external circuit to the Pt surface of counter electrode to achieve efficient photoelectrochemical hydrogen evolution from water splitting.

4. Conclusion

In summary, an O_V-BiOBr/$Cu_{2-x}S$ type I high-low junction with double defects was successfully prepared using a two-step solvothermal method. The efficient hydrogen generation performance was achieved under visible light and applied voltage. The hydrogen evolution rate could reach 509.37 $\mu mol \cdot cm^{-2} \cdot h^{-1}$, which is 12.45, 6.94 and 3.44 times that of pure BiOBr, O_V-BiOBr, and BiOBr/$Cu_{2-x}S$, respectively. For the first time, it is found that there are obvious strange active free radical phenomena in OV-BiOBr/Cu2-xS with double defects in the dark state. Theoretical and experimental results indicate that the highly dissociated domain of positive and negative charges of O_V and V_{Cu} induces interfacial polarization enhancement of the heterojunction and greatly promotes the separation and transfer of charge carriers. The boosted photoelectrochemical hydrogen evolution and high charge separation efficiency are attributed to the synergistic effect of the enhanced polarization electric field and the internal electric field of the double-defect O_V-BiOBr/$Cu_{2-x}S$ high-low junction. This work provides a feasible strategy for the development of double-defect engineering-mediated efficient carrier transport heterojunction applied in high-performance photoelectrocatalytic electrode materials.

CRediT authorship contribution statement

Xibao Li: Conceptualization, Methodology, Writing – review & editing. **Qiang Liu**: Data curation, Writing – original draft. **Fang Deng**: Writing – review & editing, Funding acquisition. **Juntong Huang:** Methodology, Data curation. **Lu Han:** Resources. **Chaozheng He:** Resources, Software. **Zhi Chen:** Data curation. **Yidan Luo:** Formal analysis. **Yongfa Zhu:** Project administration; Supervision, Conceptualization.

Declaration of Competing Interest

The authors declare that they have no known competing financial interests or personal relationships that could have appeared to influence the work reported in this paper.

Acknowledgments

Appendix A. Supporting information

Supplementary data associated with this article can be found in the online version at doi:10.1016/j.apcatb.2022.121502.

References

[1] W. Jiang, Y. An, Z. Wang, M. Wang, X. Bao, L. Zheng, H. Cheng, P. Wang, Y. Liu, Z. Zheng, Y. Dai, B. Huang, Stress-induced BiVO₄ photoanode for enhanced photoelectrochemical performance, Appl. Catal. B: Environ. 304 (2022), 121012.

[2] B. He, C. Bie, X. Fei, B. Cheng, J. Yu, W. Ho, A.A. Al-Ghamdi, S. Wageh, Enhancement in the photocatalytic activity of CdS NRs by Ag₂S and NiS dual cocatalysts, Appl. Catal. B: Environ. 288 (2021), 119994.

[3] X. Jiang, L. Zhang, H. Liu, D. Wu, F. Wu, L. Tian, L. Liu, J. Zou, S. Luo, B. Chen, Silver single atom in carbon nitride catalyst for highly efficient photocatalytic hydrogen evolution, Angew. Chem. Int. Ed. 59 (2020) 23112–23116.

[4] M.W. Kanan, D.G. Nocera, In situ formation of an oxygen-evolving catalyst in neutral water containing phosphate and Co2+, Science 321 (2008) 1072–1075.

[5] S. Lin, H. Huang, T. Ma, Y. Zhang, Photocatalytic oxygen evolution from water splitting, Adv. Sci. 8 (2021) 2002458.

[6] L. Duan, F. Bozoglian, S. Mandal, B. Stewart, T. Privalov, A. Llobet, L. Sun, A molecular ruthenium catalyst with water-oxidation activity comparable to that of photosystem II, Nat. Chem. 4 (2012) 418–423.

[7] S. Shen, S.A. Lindley, X. Chen, J.Z. Zhang, Hematite heterostructures for photoelectrochemical water splitting: rational materials design and charge carrier dynamics, Energy Environ. Sci. 9 (2016) 2744–2775.

[8] S. Dong, Y. Zhao, J. Yang, X. Liu, W. Li, L. Zhang, Y. Wu, J. Sun, J. Feng, Y. Zhu, Visible-light responsive PDI/rGO composite film for the photothermal catalytic degradation of antibiotic wastewater and interfacial water evaporation, Appl. Catal. B: Environ. 291 (2021), 120127.

[9] Y. Fu, Z. Ren, J. Wu, Y. Li, W. Liu, P. Li, L. Xing, J. Ma, H. Wang, X. Xue, Direct Z-scheme heterojunction of ZnO/MoS₂ nanoarrays realized by flowing-induced piezoelectric field for enhanced sunlight photocatalytic performances, Appl. Catal. B: Environ. 285 (2021) 119785.

[10] X. Li, W. Wang, F. Dong, Z. Zhang, L. Han, X. Luo, J. Huang, Z. Feng, Z. Chen, G. Jia, T. Zhang, Recent advances in noncontact external-field-assisted photocatalysis: from fundamentals to applications, ACS Catal. 11 (2021) 4739–4769.

[11] Y. Xi, X. Zhang, Y. Shen, W. Dong, Z. Fan, K. Wang, S. Zhong, S. Bai, Aspect ratio dependent photocatalytic enhancement of CsPbBr₃ in CO₂ reduction with two-dimensional metal organic framework as a cocatalyst, Appl. Catal. B: Environ. 297 (2021), 120411.

[12] Y. Xi, Y. Zhang, X. Cai, Z. Fan, K. Wang, W. Dong, Y. Shen, S. Zhong, L. Yang, S. Bai, PtCu thickness-modulated interfacial charge transfer and surface reactivity in stacked graphene/Pd@PtCu heterostructures for highly efficient visible-light reduction of CO₂ to CH₄, Appl. Catal. B: Environ. 305 (2022), 121069.

[13] J. Zhang, T. Bai, H. Huang, M. Yu, X. Fan, Z. Chang, X. Bu, Metal–organic-framework-based photocatalysts optimized by spatially separated cocatalysts for overall water splitting, Adv. Mater. 32 (2020) 2004747.

[14] Y. Xi, W. Chen, W. Dong, Z. Fan, K. Wang, Y. Shen, G. Tu, S. Zhong, S. Bai, Engineering an interfacial facet of S-scheme heterojunction for improved photocatalytic hydrogen evolution by modulating the internal electric field, ACS Appl. Mater. Interfaces 13 (2021) 39491–39500.

[15] H. Lyu, T. Hisatomi, Y. Goto, M. Yoshida, T. Higashi, M. Katayama, T. Takata, T. Minegishi, H. Nishiyama, T. Yamada, Y. Sakata, K. Asakura, K. Domen, An Al-doped SrTiO₃ photocatalyst maintaining sunlight-driven overall water splitting activity for over 1000h of constant illumination, Chem. Sci. 10 (2019) 3196–3201.

[16] S. Dong, L. Cui, Y. Tian, L. Xia, Y. Wu, J. Yu, D.M. Bagley, J. Sun, M. Fan, A novel and high-performance double Z-scheme photocatalyst ZnO-SnO₂-Zn₂SnO₄ for effective removal of the biological toxicity of antibiotics, J. Hazard. Mater. 399 (2020), 123017.

[17] L. Hao, H. Huang, Y. Zhang, T. Ma, Oxygen vacant semiconductor photocatalysts, Adv. Funct. Mater. 31 (2021) 2100919.

[18] X. Li, B. Kang, F. Dong, Z. Zhang, X. Luo, L. Han, J. Huang, Z. Feng, Z. Chen, J. Xu, B. Peng, Z.L. Wang, Enhanced photocatalytic degradation and H₂/H₂O₂ production performance of S-pCN/WO₂.₇₂ S-scheme heterojunction with appropriate surface oxygen vacancies, Nano Energy 81 (2021), 105671.

[19] S. Wang, T. He, P. Chen, A. Du, K. Ostrikov, W. Huang, L. Wang, In situ formation of oxygen vacancies achieving near-complete charge separation in planar BiVO₄ photoanodes, Adv. Mater. 32 (2020) 2001385.

[20] Z. Wei, W. Wang, W. Li, X. Bai, J. Zhao, E.C.M. Tse, D.L. Phillips, Y. Zhu, Steering electron–hole migration pathways using oxygen vacancies in tungsten oxides to enhance their photocatalytic oxygen evolution performance, Angew. Chem. Int. Ed. 60 (2021) 8236–8242.

[21] L. Zhang, X. Xue, T. Guo, L. Bi, T. Hu, L. Tan, X. Zhang, J. Jiang, K. Hong, Q. Zhang, Creation of oxygen vacancies to activate Fe₂O₃ photoanode by simple solvothermal method for highly efficient photoelectrochemical water oxidation, Int. J. Hydrog. Energy 46 (2021) 12897–12905.

[22] S. Ye, C. Ding, M. Liu, A. Wang, Q. Huang, C. Li, Water oxidation catalysts for artificial photosynthesis, Adv. Mater. 31 (2019) 1902069.

[23] Z. Wang, C. Li, K. Domen, Recent developments in heterogeneous photocatalysts for solar-driven overall water splitting, Chem. Soc. Rev. 48 (2019) 2109–2125.

[24] F. Xu, K. Meng, S. Cao, C. Jiang, T. Chen, J. Xu, J. Yu, Step-by-step mechanism insights into the TiO$_2$/Ce$_2$S$_3$ S-Scheme photocatalyst for enhanced aniline production with water as a proton source, ACS Catal. 12 (2022) 164–172.

[25] X. Li, Q. Luo, L. Han, F. Deng, Y. Yang, F. Dong, Enhanced photocatalytic degradation and H$_2$ evolution performance of NCDs/S-C$_3$N$_4$ S-scheme heterojunction constructed by π-π conjugate self-assembly, J. Mater. Sci. Technol. 114 (2022) 222–232.

[26] H. Li, F. Deng, Y. Zheng, L. Hua, C. Qu, X. Luo, Visible-light-driven Z-scheme rGO/ Bi2S3-BiOBr heterojunctions with tunable exposed BiOBr (102) facets for efficient synchronous photocatalytic degradation of 2-nitrophenol and Cr(VI) reduction, Environ. Sci.: Nano 6 (2019) 3670–3683.

[27] S. Dong, L. Xia, X. Chen, L. Cui, W. Zhu, Z. Lu, J. Sun, M. Fan, Interfacial and electronic band structure optimization for the adsorption and visible-light photocatalytic activity of macroscopic ZnSnO$_3$/graphene aerogel, Compos. Part B: Eng. 215 (2021), 108765.

[28] N. Sun, Y. Qu, C. Yang, Z. Yang, R. Yan, W.E.Z. Zhang, Z. Li, H. Li, I. Khan, R. Sun, L. Jing, H. Fu, Efficiently photocatalytic degradation of monochlorophenol on in-situ fabricated BiPO4/β-Bi2O3 heterojunction microspheres and O2-free hole-induced selective dechloridation conversion with H$_2$ evolution, Appl. Catal. B: Environ. 263 (2020), 118313.

[29] L. Guo, Y. Chen, Z. Ren, X. Li, Q. Zhang, J. Wu, Y. Li, W. Liu, P. Li, Y. Fu, J. Ma, Morphology engineering of type-II heterojunction nanoarrays for improved sonophotocatalytic capability, Ultrason. Sonochem. 81 (2021), 105849.

[30] Z. Yang, L. Shao, L. Wang, X. Xia, Y. Liu, S. Cheng, C. Yang, S. Li, Boosted photogenerated carriers separation in Z-scheme Cu$_3$P/ZnIn2S$_4$ heterojunction photocatalyst for highly efficient H$_2$ evolution under visible light, Int. J. Hydrog. Energy 45 (2020) 14334–14346.

[31] D. Gogoi, A.K. Shah, P. Rambabu, M. Qureshi, A.K. Golder, N.R. Peela, Step-scheme heterojunction between CdS nanowires and facet-selective assembly of MnO$_x$- BiVO$_4$ for an efficient visible-light-driven overall water splitting, ACS Appl. Mater. Interfaces 13 (2021) 45475–45487.

[32] M. Huang, X. Wang, G. Xing, C. Meng, Y. Li, X. Li, L. Fan, Y. Wan, S. Yang, Plasmonic hot hole extraction from CuS nanodisks enables significant acceleration of oxygen evolution reactions, J. Phys. Chem. Lett. 12 (2021) 7988–7996.

[33] X. Tong, X. Cao, T. Han, W. Cheong, R. Lin, Z. Chen, D. Wang, C. Chen, Q. Peng, Y. Li, Convenient fabrication of BiOBr ultrathin nanosheets with rich oxygen vacancies for photocatalytic selective oxidation of secondary amines, Nano Res. 12 (2019) 1625–1630.

[34] J. Zhu, Y. Li, X. Wang, J. Zhao, Y. Wu, F. Li, Simultaneous phosphorylation and Bi modification of BiOBr for promoting photocatalytic CO$_2$ reduction, ACS Sustain. Chem. Eng. 7 (2019) 14953–14961.

[35] Z. Zhao, Y. Cao, F. Dong, F. Wu, B. Li, Q. Zhang, Y. Zhou, The activation of oxygen through oxygen vacancies in BiOCl/PPy to inhibit toxic intermediates and enhance the activity of photocatalytic nitric oxide removal, Nanoscale 11 (2019) 6360–6367.

[36] Q. Wang, Z. Liu, D. Liu, G. Liu, M. Yang, F. Cui, W. Wang, Ultrathin two-dimensional BiOBr$_x$I$_{1-x}$ solid solution with rich oxygen vacancies for enhanced visible-light-driven photoactivity in environmental remediation, Appl. Catal. B: Environ. 236 (2018) 222–232.

[37] X. Huang, G. Deng, Y. Han, G. Yang, R. Zou, Z. Zhang, S. Sun, J. Hu, Right Cu$_{2-x}$S@ MnS core–shell nanoparticles as a Photo/H$_2$O$_2$-responsive platform for effective cancer theranostics, Adv. Sci. 6 (2019) 1901461.

[38] L. Jiang, K. Wang, X. Wu, G. Zhang, Highly enhanced full solar spectrum-driven photocatalytic CO$_2$ reduction performance in Cu$_{2-x}$S/g-C$_3$N$_4$ composite: Efficient charge transfer and mechanism insight, Sol. RRL 5 (2021) 2000326.

[39] Y. Qiu, Z. Xing, M. Guo, Z. Li, N. Wang, W. Zhou, Hollow cubic Cu$_{2-x}$S/Fe-POMs/ AgVO$_3$ dual Z-scheme heterojunctions with wide-spectrum response and enhanced photothermal and photocatalytic-fenton performance, Appl. Catal. B: Environ. 298 (2021) 120628.

[40] D. Zhou, D. Liu, W. Xu, Z. Yin, X. Chen, P. Zhou, S. Cui, Z. Chen, H. Song, Observation of considerable upconversion enhancement induced by Cu$_{2-x}$S plasmon nanoparticles, ACS Nano 10 (2016) 5169–5179.

[41] Z. Long, G. Zhang, H. Du, J. Zhu, J. Li, Preparation and application of BiOBr-Bi$_2$S$_3$ heterojunctions for efficient photocatalytic removal of Cr(VI), J. Hazard. Mater. 407 (2021), 124394.

[42] H. Li, T. Hu, N. Du, R. Zhang, J. Liu, W. Hou, Wavelength-dependent differences in photocatalytic performance between BiOBr nanosheets with dominant exposed (001) and (010) facets, Appl. Catal. B: Environ. 187 (2016) 342–349.

[43] X. Wu, Y.H. Ng, L. Wang, Y. Du, S.X. Dou, R. Amal, J. Scott, Improving the photo-oxidative capability of BiOBr via crystal facet engineering, J. Mater. Chem. A 5 (2017) 8117–8124.

[44] M. Shi, G. Li, J. Li, X. Jin, X. Tao, B. Zeng, E.A. Pidko, R. Li, C. Li, Intrinsic facet-dependent reactivity of well-defined BiOBr nanosheets on photocatalytic water splitting, Angew. Chem. Int. Ed. 59 (2020) 6590–6595.

[45] H. Yu, F. Chen, X. Li, H. Huang, Q. Zhang, S. Su, K. Wang, E. Mao, B. Mei, G. Mul, T. Ma, Y. Zhang, Synergy of ferroelectric polarization and oxygen vacancy to promote CO$_2$ photoreduction, Nat. Commun. 12 (2021) 4594.

[46] X. Dong, W. Zhang, Y. Sun, J. Li, W. Cen, Z. Cui, H. Huang, F. Dong, Visible-light-induced charge transfer pathway and photocatalysis mechanism on Bi semimetal@ defective BiOBr hierarchical microspheres, J. Catal. 357 (2018) 41–50.

[47] Y.T. Kwon, G.D. Lim, S. Kim, S.H. Ryu, H.R. Lim, Y.H. Choa, Effect of localized surface plasmon resonance on dispersion stability of copper sulfide nanoparticles, Appl. Surf. Sci. 477 (2019) 204–210.

[48] J. Xiong, X. Li, J. Huang, X. Gao, Z. Chen, J. Liu, H. Li, B. Kang, W. Yao, Y. Zhu, CN/rGO@BPQDs high-low junctions with stretching spatial charge separation ability for photocatalytic degradation and H$_2$O$_2$ production, Appl. Catal. B: Environ. 266 (2020), 118602.

[49] L. Zhou, Z. Liu, Z. Guan, B. Tian, L. Wang, Y. Zhou, Y. Zhou, J. Lei, J. Zhang, Y. Liu, 0D/2D plasmonic Cu$_{2-x}$S/g-C$_3$N$_4$ nanosheets harnessing UV–vis-NIR broad spectrum for photocatalytic degradation of antibiotic pollutant, Appl. Catal. B: Environ. 263 (2020), 118326.

[50] S.G. Shim, J. Tan, H. Lee, J. Park, J. Yun, Y.S. Park, K. Kim, J. Lee, J. Moon, Facile morphology control strategy to enhance charge separation efficiency of Mo:BiVO$_4$ photoanodes for efficient photoelectrochemical water splitting, Chem. Eng. J. 430 (2022), 133061.

[51] M. Huang, H. Wang, H. Li, Y. Zhao, R. Zhang, In situ textured carbon nitride photoanodes with enhanced photoelectrochemical activity by band-gap state modulation, J. Mater. Chem. A 8 (2020) 24005–24012.

[52] H. Sun, W. Hua, Y. Li, J. Wang, Promoting photoelectrochemical activity and stability of WO$_3$/BiVO$_4$ heterojunctions by coating a tannin nickel iron complex, ACS Sustain. Chem. Eng. 8 (2020) 12637–12645.

[53] H. Chen, S. Wang, J. Wu, X. Zhang, J. Zhang, M. Lyu, B. Luo, G. Qian, L. Wang, Identifying dual functions of rGO in a BiVO$_4$/rGO/NiFe-layered double hydroxide photoanode for efficient water splitting, J. Mater. Chem. A 8 (2020) 13231–13240.

[54] S.S. Yi, B.R. Wulan, J.M. Yan, Q. Jiang, Highly efficient photoelectrochemical water splitting: surface modification of cobalt-phosphate-loaded Co$_3$O$_4$/Fe$_2$O$_3$ p–n heterojunction nanorod arrays, Adv. Funct. Mater. 29 (2019) 1801902.

[55] Y. Li, J. Wang, Y. Fan, H. Sun, W. Hua, H. Liu, B. Wei, Plasmonic TiN boosting nitrogen-doped TiO$_2$ for ultrahigh efficient photoelectrochemical oxygen evolution, Appl. Catal. B: Environ. 246 (2019) 21–29.

[56] S. Wang, T. He, J. Yun, Y. Hu, M. Xiao, A. Du, L. Wang, New iron-cobalt oxide catalysts promoting BiVO$_4$ films for photoelectrochemical water splitting, Adv. Funct. Mater. 28 (2018) 1802685.

[57] C. Huang, S. Shi, H. Yu, Work function adjustment of Nb$_2$CT$_x$ nanoflakes as hole and electron transport layers in organic solar cells by controlling surface functional groups, ACS Energy Lett. 6 (2021) 3464–3472.

[58] J. He, Y. Zhao, S. Jiang, S. Song, Photocatalysis within intrinsic spontaneous polarization electric field, Sol. RRL 5 (2021) 2000446.